Wall-based reduced order modelling

Lasagna D., Tutty O. R.

Abstract

In this work we propose a novel approach to model order reduction for incompressible fluid flows that focuses on the spatio-temporal description of the stresses on the surface of a body, i.e. of the wall shear stress and of the wall pressure. The spatial representation of these two variables is given by a compact set of "wall basis functions", i.e. elementary basis functions defined on the wall. In this paper, these are derived using the well-known Proper Orthogonal Decomposition, to represent optimally the fluctuation energy of the pressure and shear stress. On the other hand, the functional structure of the dynamic model is derived from first principles using the vorticity form of the Navier-Stokes equations, yielding a set of nonlinear ordinary differential equations for the time-varying amplitudes of the wall shear stress basis functions. Coefficients of this model are then identified from simulation data. To complete the system, we show that the surface pressure distribution, i.e. the time-varying amplitudes of the wall pressure basis functions, can be derived from a quadratic model of the wall shear stress temporal coefficients, stemming from the Poisson equation for the pressure. This further step is crucial for the correct representation of the aerodynamic forces. As a paradigmatic example, we present our approach for the modelling of the free dynamics of the separated flow around a circular cylinder in the laminar regime, at $Re = 200$. Further implications and potentialities of the proposed approach are discussed.

1 Introduction

It is generally accepted that relying on heuristic or trial-and-error approaches to design flow control strategies for fluid systems often results in poor performances (1). Hence, attempts to apply rigorous approaches rooted into control theory have been proposed in the last few decades to design more effective and more efficient controllers, see for example the review of Kim & Bewley (2). However, it is widely acknowledged (3), that the wide range of temporal and spatial scales that distinguishes the motion of turbulent flows leads to systems of extremely high dimensionality, such that their treatment is feasible only at Reynolds numbers orders of magnitude lower those commonly found in engineering and industrial applications.

Nevertheless, a new trend in research in fluid mechanics in the last few decades has been motivated by the observation that large-scale, energy-dominant dynamics are pervasive in turbulent flows and that targeting their control is often sufficient to obtain adequate performances (4). As a result, model order reduction techniques, whereby the large scales dynamics are first identified and isolated, have been developed considerably. A widely known approach is based on the Galerkin projection method. In this method, a set of ad-hoc global basis functions, that represent elementary flow fields describing the large scale dynamics, is first derived. The governing partial differential equations are then reduced, by projection, to a system of ordinary differential equations for the

time-varying amplitudes of these basis functions. Compression of the dimensionality of the dynamics by several orders of magnitude, without sacrificing the accuracy of the representation is usually possible, opening the road to effective design of reduced order controllers.

However, there are still a number of outstanding issues inherent in this methodology that hinder its application to flows of engineering interest (5), while laboratory investigations using these methods are also rare (6). One fundamental issue is that the dominant coherent structures have to be first identified. For data based methods, that provide empirical basis functions, e.g for the well-known Proper Orthogonal Decomposition (POD) (7), this preliminary step usually requires costly and time-consuming direct numerical simulations or highly-resolved experimental measurements. For complex, three-dimensional flows at high Reynolds number, or for applications where limited or no access to the region of interest is available, this first step is often prohibitive. This is aggravated in the case where the POD basis functions needs to be iteratively updated as a result of application of flow control, (8; 9; 10), because the flow dynamics might be so severely perturbed that the basis functions derived in no-control conditions might have a reduced ability to describe the forced dynamics (11; 12).

A second fundamental issue is that related to the system state reconstruction from limited and noisy wall information, that is the observer design problem. This problem is still reckoned as an outstanding issue (3), and progress in this direction is still required. Examples of works investigating this aspect are those of Podvin & Lumley (13), Hœpffner et al. (14) and Jones et al. (15) for wall bounded flows; the works of Lehmann et al. (12) and Buffoni et al. (16) for bluff body flows, and the studies of Rowley & Juttijudata (17) and Nagarajan et al. (18) for cavity flows.

In this paper we present a novel approach that helps to alleviate some of these drawbacks. The fundamental idea is to obtain a predictive model that does not target directly the dynamics of the large scale structures in the flow but which achieves the same result by describing only their effects on the surface of the body. The complete signature, or the footprint, of these coherent structure is given by the spatio-temporal surface distributions of the stresses at the wall, which is, incidentally, what is needed to accurately describe the unsteady forces acting on the body, a matter of fundamental interest in engineering applications.

The derivation of the proposed methodology is based on two observations. The first observation relates to the basic fact that the wall shear stress is proportional to the value of the vorticity at the wall, indicating that the large scale vortex dynamics in more or less close proximity of the body can be readily identified by the effects they induce on the wall shear stress distribution. Hence, based on the vorticity form of the governing Navier-Stokes equations, we will derive the functional structure of a reduced order model (ROM) that describes the spatio-temporal evolution of the surface distribution of the wall shear stress. Unlike methods based on input-output modelling, (19; 20; 21), or based on black-box structures, (22), this functional structure is based on a first-principles derivation. The second observation relates to the fact that pressure commonly represents the dominant contribution to the aerodynamic forces and, thus, needs to be integrated in the model. Bergmann and Cordier, (8), included the pressure contribution, hence obtaining accurate low-order force estimation, by employing an extended velocity-pressure POD basis to derive the low-order models. In the present work, we adopt a different method, building on the ideas of Galletti et al. (23) and Noack et al. (24), which showed how the projection of the velocity basis functions on the pressure gradient term in the Galerkin projection of the Navier-Stokes can be modelled using linear of quadratic functionals of the velocity modes amplitudes. However, as opposed to these works, we do not use these models to correct the dynamics of the low order systems, because they originate from the vorticity equation, where pressure does not appear. Instead, we use the same structure to

estimate the surface pressure distribution around the body, from the wall shear stress distribution, which in turn is used to compute the contribution to the forces due to the wall pressure.

The stringent requirement of possessing the detailed time-dependent picture of the entire flow field is significantly relaxed by adopting this perspective. The only requirement to obtain an accurate model is the availability of measurements on the surface of the body resolved in space and time to a point which is sufficient to uniquely identify the large scale dynamics. Crucially, obtaining these data in experiments is significantly easier than performing field measurements. This is one of the main motivation for investigating wall-based models.

In this paper, to demonstrate the validity of this methodology, we apply it to the paradigmatic example of modelling the aerodynamic forces acting on a circular cylinder in the two-dimensional laminar regime, at a Reynolds number equal to 200. This oscillatory flow, dominated by an absolute instability and globally synchronised dynamics, has been the subject of extensive studies concerning model order reduction, (25; 26; 23; 27), and control design using reduced order models, (28; 29; 30). Hence, this flow represents a rich benchmark problem to assess the advantages and the disadvantages of the proposed technique. We do not consider the case of the flow with surface actuation as it is beyond the scope of this paper and would depend on the form of the actuation employed.

The paper is structured as follows. In section 2 a description of the setup used to solve the numerical problem is presented, together with a brief validation analysis. Subsequently, the steps required to arrive at a working model of the surface distributions of the wall shear stress and the wall pressure around the cylinder are outlined in section 3, using first-principle arguments. Each step is illustrated by numerical results, presented to demonstrate the approach. A separate section, section 4, presents an analysis that focuses on showing the relation between the surface distribution of the shear stress and the spatial structure of vorticity basis functions obtained from application of POD on the full flow field. Finally, the potentialities, issues and perspectives of the proposed method are summarised in the concluding section.

2 Numerical setup

2.1 Definitions and numerical model

The formulation used in the present analysis to solve the flow problem is based on the Navier-Stokes momentum equation for a two-dimensional incompressible viscous fluid, which reads as

$$\frac{\partial \boldsymbol{u}}{\partial t} = -\boldsymbol{u} \cdot \nabla \boldsymbol{u} - \nabla p + \frac{1}{Re} \nabla^2 \boldsymbol{u}, \tag{1}$$

complemented by the continuity constraint

$$\nabla \cdot \boldsymbol{u} = 0, \tag{2}$$

where $\boldsymbol{u} = u\boldsymbol{i} + v\boldsymbol{j}$ is the velocity vector defined on a two-dimensional Cartesian space $\boldsymbol{x} = x\boldsymbol{i} + y\boldsymbol{j}$, and p is the pressure differential with respect to the far field pressure. Normalisation of the governing equations, resulting in (1, 2), is done using the cylinder diameter and the free stream velocity. This yields a definition of the Reynolds number as $Re = u_\infty D/\nu$, where D is the cylinder diameters, u_∞ is the free stream velocity and ν is the kinematic viscosity of the fluid.

As sketched in the cartoon of figure 1 the Cartesian reference frame is centred on the centre of the cylinder, located at $\boldsymbol{x} = (0, 0)$, and oriented such that the x axis is aligned with the free

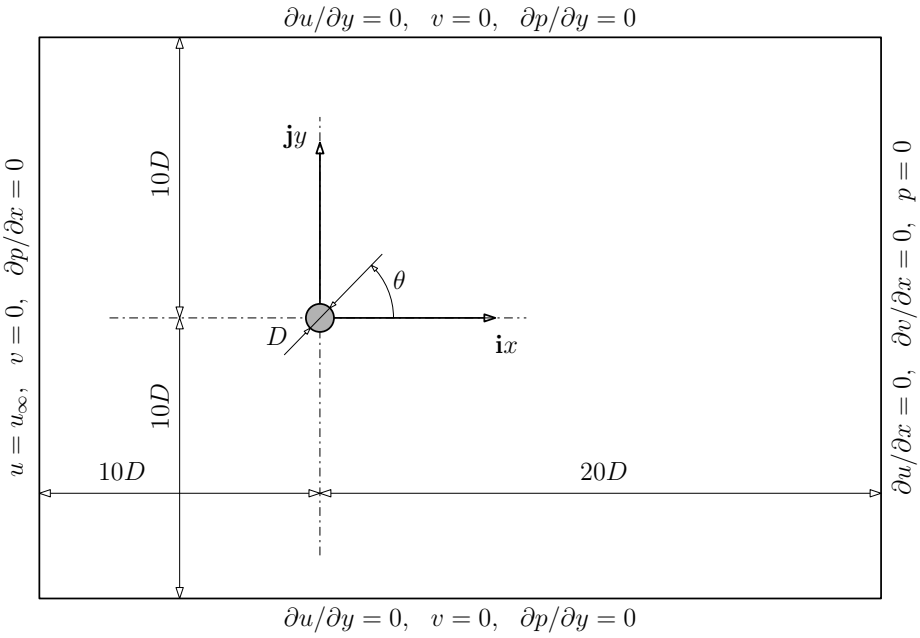

Figure 1: Schematic of the problem configuration for the circular cylinder flow. Boundary conditions on the outer domain boundaries are also indicated.

stream. Unless stated otherwise in the text, the angle θ, used in the following to denote the angular coordinate over the surface of the cylinder, originates from the unit vector $\boldsymbol{i}$ and is positive when taken counter-clockwise.

The Navier-Stokes problem (1, 2) is solved on a triangular unstructured mesh with a finite volume formulation provided by the open source code OpenFOAM (31). A mesh of intermediate fineness, mesh M2 in table 1 with $h_{wall} = 0.01$, (the size of the elements adjacent to the cylinder), is shown in the left-most panel of figure 2. The application `icofoam`, implementing the well-known PISO algorithm has been used to solve the velocity-pressure coupling (32).

The computational domain is rectangular and extends for 10 and 20 diameters upstream and downstream of the cylinder, respectively, and spans a total vertical size of 20 diameters. The domain has the same size as the one used by Bergmann et al (30) for the same flow problem. The boundary conditions associated with the problem are also sketched in figure 1. At the inflow, the Dirichlet condition $\boldsymbol{u} = (u_\infty, 0)$ is used for the velocity, while the Neumann condition $\partial p/\partial x = 0$ is used for the pressure. On the upper and bottom boundaries a free-slip condition is used for the velocity, such that $\partial u/\partial y = 0$ and $v = 0$. A zero gradient condition is used for the pressure on these two boundaries. On the cylinder surface the no-slip condition $\boldsymbol{u} = (0, 0)$ is enforced, while the standard zero normal pressure gradient condition is used for the pressure. At the outflow boundary, good numerical results, without spurious reflections from the boundary, were obtained by using a zero normal gradient condition for the velocity, i.e. $\partial \boldsymbol{u}/\partial x = (0, 0)$, while the Dirichlet condition $p = 0$ was set to fix uniquely the pressure field.

The time step was set constant and equal to $\Delta t = 0.0025$ for a fine mesh used to obtain all the results reported in the rest of the paper, (mesh M2 in table 1). This choice was adopted to achieve

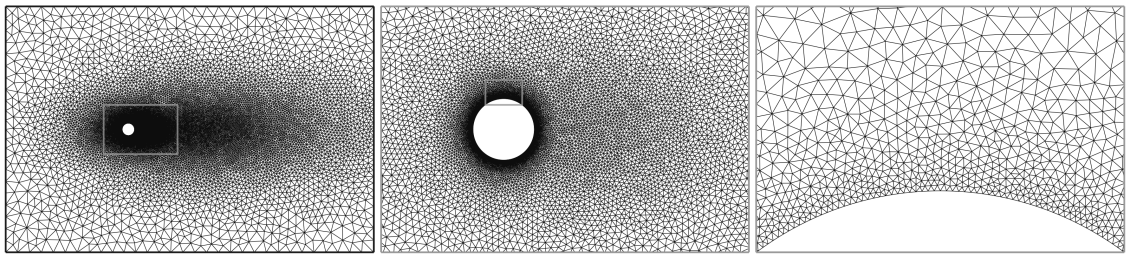

Figure 2: Computational domain and complete grid for a typical mesh with $h_{wall} = 0.01$, left; near-cylinder close-up, centre; near-wall close-up, right.

satisfactory temporal resolution and a maximum Courant number in the flow field of the order of 0.7. We observed that the flow reached the stationary periodic conditions after a short-lived transient of about 80 time units. Snapshots were then collected from $t \geq 100$ to $t = 300$, i.e. over about 40 shedding cycles, at time intervals of 0.1, to resolve accurately all important frequencies.

The wall distributions of the pressure and shear stress variables are denoted $p(t, \theta)$ and $\tau(t, \theta)$, respectively. The wall shear stress is assumed positive when the viscous force would induce a counter-clockwise rotation of the cylinder, and negative otherwise. Furthermore, in what follows, we will use the non-dimensional pressure p directly, instead of introducing a pressure coefficient, and similarly for the wall shear stress.

The aerodynamic forces, obtained by summing the pressure and viscous contributions, are normalised by $1/2\rho u_\infty^2 D$, where ρ is the fluid density. This yields definitions of drag and lift force coefficients as

$$C_D(t) = -\int_0^{2\pi} p(t,\theta)\cos\theta \mathrm{d}\theta - \int_0^{2\pi} \tau(t,\theta)\sin\theta \mathrm{d}\theta \tag{3}$$

and

$$C_L(t) = -\int_0^{2\pi} p(t,\theta)\sin\theta \mathrm{d}\theta + \int_0^{2\pi} \tau(t,\theta)\cos\theta \mathrm{d}\theta, \tag{4}$$

respectively, obtained by integration with the trapezoidal rule from wall distributions sampled from simulation.

Preliminary validation and grid convergence studies have been conducted to asses the reliability of the solver. Mesh independence is assessed by evaluating the effect of the mesh density on the time averaged drag coefficient $\overline{C}_D$, on the Strouhal number $S_t = f_{sh}D/u_\infty$, with f_{sh} the shedding frequency, and on half the peak to peak amplitude of the lift coefficient fluctuations C_L^A, which are quantities commonly reported in the literature for this problem. The computational parameters and the simulation results obtained with three different meshes, with different h_{wall}, are listed in table 1. It can be seen that all the integral quantities show a satisfactory level of convergence at least since the intermediate mesh M2. In addition, the integral quantities are in close agreement with results obtained by several other authors, using different numerical setups. Hence, data from the simulation with mesh M2 has been used for further post-processing and for all the results presented in this paper.

Authors	h_{wall}	N_{cells}	N_{nodes}	$\overline{C}_D$	S_t	C_L^A
Present - Mesh M1	0.02	29658	14968	1.37	0.198	0.69
Present - Mesh M2	0.01	62098	31269	1.39	0.199	0.70
Present - Mesh M3	0.005	130252	65506	1.39	0.199	0.70
Franke et al. - (33)				1.31	0.194	0.65
He et al. - (34)				1.36	0.198	0.69
Bergmann et al - (30)		25000	12686	1.39	0.200	
Wang et al. - (35)				1.36	0.195	0.71
Lu et al. - (36)				1.34	0.196	0.69

Table 1: Grid parameters and numerical results for the grid convergence studies. Comparison with other published results is also shown when available.

3 Wall-based modelling

We begin with a preliminary discussion related to the temporal and spatial structure of the surface distributions of the two quantities of interest. The core ideas and the steps of the wall-based modelling approach are then reported.

3.1 Mean and space-time surface distributions

Time-averaged, (solid line), and root-mean-square, (dash-dotted line), distributions of the wall shear stress and of the wall pressure are reported in the panels (a) and (b) of figure 3, respectively. For the sake of clarity, the absolute value of the mean wall shear stress has been reported, with a dashed line indicating negative values, while the root-mean-square distribution has been scaled by a factor of five for both pressure and shear stress, for readability.

The mean flow separation angle is located at $\theta_{sep} = 66$, in relatively good agreement with other numerical results at the same Reynolds number (see e.g. (33; 37)). The shear stress distribution indicates that the larger mean values occur somewhere halfway between the stagnation and the separation points, with relatively low mean values after separation, in the region of reverse flow. However, the largest fluctuations are observed in the rear part of the cylinder. Observation of animated flow sequences indicate that these large fluctuations are due to the intense vorticity structures periodically generated in the near-wake region by the vortex shedding, in close vicinity to the cylinder. Relatively intense wall shear stress fluctuations are also observed around $\theta = \pm\pi/2$, slightly before the separation point.

For pressure, the mean distribution agrees relatively well with results published in the literature, for the same Reynolds number (38), even though our value of the mean stagnation pressure is around 5% larger than that obtained in the cited reference. The distribution of the root-mean-square value of the wall pressure fluctuations indicates that the most intense fluctuations occur at $\theta = \pm\pi/2$. This result agrees with the observation that the fluctuations of the lift are, in general, much larger than those of the drag force (39).

The time-averaged statistics reported in figure 3 fail to convey the required insight into the dynamics of the spatio-temporal fluctuations on the whole surface of the cylinder. For this reason, we report in panels (a) and (b) of figure 4 time-space diagrams of the fluctuations of the wall shear stress and of the wall pressure, respectively. The time scale spans about four shedding

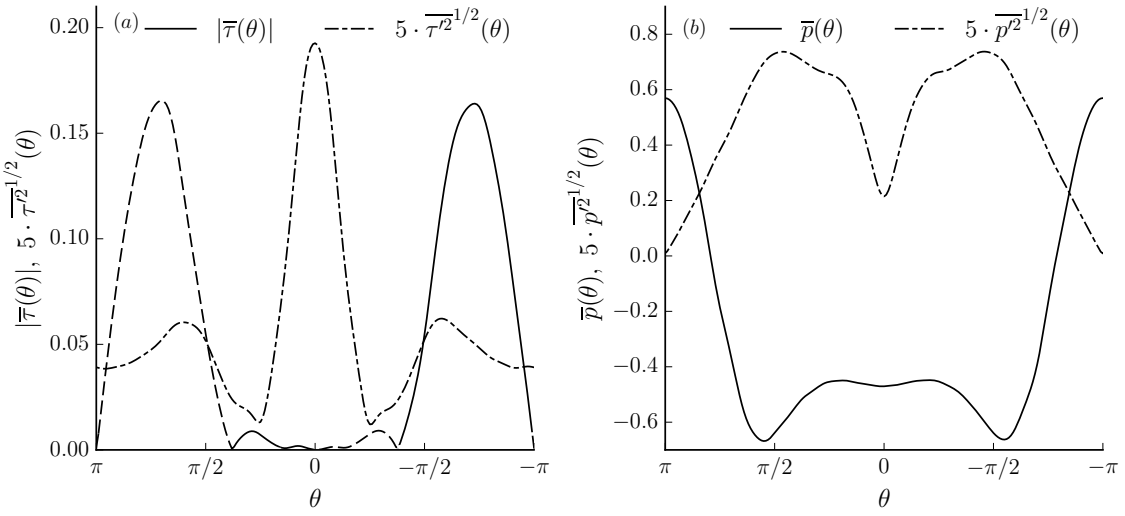

Figure 3: (a): absolute value of mean, (solid line), and root-mean-square value, (dashed-dot) line, distributions of the wall shear stress. Negative values for the mean distribution are indicated by a dashed line. (b): same quantities for the wall pressure. The distributions are reported as a function of the angle θ, whose origin is set at the rear point of the cylinder.

cycles, starting from $t_0 = 100$. The diagram clearly highlights that a very coherent spatio-temporal structure exists on the surface of the cylinder, with a strong coupling and synchronisation between the wall pressure and the wall shear stress. We also observe that the spatial structure is dominated by large spatial scale features, and repeats periodically in time. Crucially, the availability of a model that predicts the large scale features of this spatio-temporal structure would enable in a straightforward manner the prediction of the unsteady forces on the cylinder.

3.2 Reduced order modelling by wall-based POD

We assume that the spatio-temporal distributions of both the wall pressure $p(t, \theta)$ and the wall shear stress $\tau(t, \theta)$ are available in the form of M flow snapshots containing readings from N_s sensors located on the cylinder surface. Very well spatially resolved distributions of these quantities are readily available from full-order numerical simulations, while in a laboratory experiment, these distributions could be obtained relatively easily by wall-mounted sensors. The number of sensors must be sufficiently large to provide an adequate spatial resolution of the signature of the relevant flow structures on the wall, and to provide a relatively accurate estimate of the force coefficients upon spatial integration. Furthermore, although not discussed in this paper, the position of the sensors could be chosen with an optimisation process to provide a more accurate or robust representation of the spatial structure of the fluctuations at the wall, following ideas similar to those reported by Cohen et al. (40) or by Willcox (41).

Model order reduction comes into play within the current formulation in two different ways. The first order reduction is inherent in the fact that consideration of the evolution of the flow is restricted to its footprint at the wall exclusively, whereas the dynamics in the rest of the domain

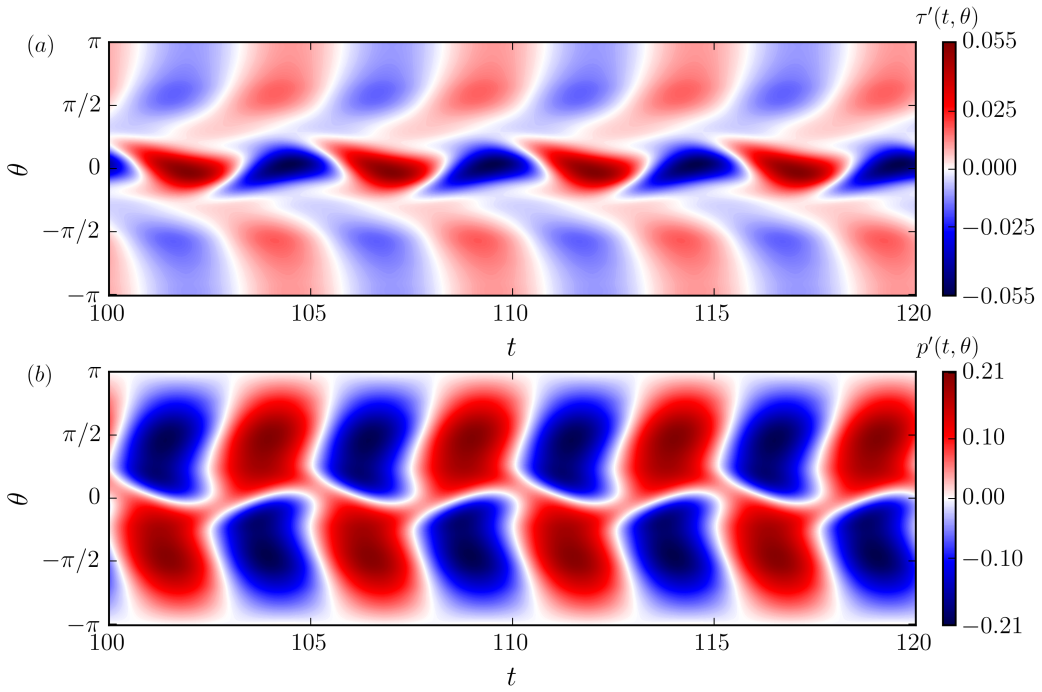

Figure 4: Time-space diagrams of the wall shear stress, (a), and wall pressure, (b), fluctuations, over a time span of about four shedding cycles.

and far away from the wall are not taken into account directly. As a result, a first strong reduction of dimensionality results by the implicit truncation of those flow structures which do not influence the surface distribution and that do not impact directly the forces.

It may be argued that some of the fundamental flow physics may be neglected using the wall-based approach described here. For example, this would be the case in flows where unobservable modes have a strong dynamical impact even tough their signature is weak or null on the wall. For example, Kim and Bewley (2) clearly show that a significant number of leading eigenmodes of the Orr-Sommerfield/Squire operator for the turbulent channel flow have very limited support at the wall, and they are thus not easily observable nor controllable by wall mounted sensors and actuators. As it is discussed in more depth later, this behaviour might prevent a correct identification of a dynamic model.

In a similar vein, the implicit truncation of flow structure which do not influence the force is analogous to that of highly truncated low order Galerkin models, of which the circular cylinder problem in the laminar regime is a well-known example (42). In these cases, the unresolved small scale features of the flow have a crucial dynamical role as they represent the energy dissipation, but are often truncated by the order reduction. These truncated models often display drifts, long-term instabilities of other unphysical solutions not pertinent to the full order system described by the original infinite-dimensional partial differential equations. A turbulence closure, or model calibration, that models the unresolved cascade of energy is then required (43; 44; 45; 46; 10; 47; 5).

The second and more controllable way where dimensionality reduction is introduced is how the surface distributions are represented. We assume that the distributions can be represented by separating the time and space variables into a linear combination of a few "wall basis functions" as

$$p(t,\theta) \backsimeq p_0(\theta) + \sum_{i=1}^{N_p} a_i^p(t) p_i(\theta) \quad \text{and} \quad \tau(t,\theta) \backsimeq \tau_0(\theta) + \sum_{i=1}^{N_\tau} a_i^\tau(t) \tau_i(\theta) \tag{5}$$

where we have adopted a decomposition using the known time-averaged distributions $p_0(\theta)$ and $\tau_0(\theta)$ implying that $a_0^p(t) = a_0^\tau(t) = 1$, while we have expanded the fluctuating components into a weighted sum of the wall basis functions and the associated temporal coefficients.

For model reduction purposes, the number of wall basis functions N_p and N_τ, which do not need to be equal, is small compared to the number of sensors N_s but is sufficiently large that the basis functions correctly describe the large-scale fluctuations. Among the numerous possible ways to derive the wall basis functions $p_i(\theta)$ and $\tau_i(\theta)$, we use in this paper the Proper Orthogonal Decomposition. Although, these basis functions do not have a dynamical meaning (48), they approximate optimally the energy of the wall fluctuations, so that the amplitude of the unsteady forces on the cylinder is optimally represented.

Because $M \gg N_s$, the classical POD method, described in Berkooz et al. (7) can be used, instead of the snapshot method described by Sirovich (49), which is widely used when $N_s \gg M$. With the definition of the inner product between two scalar functions defined on the cylinder wall

$$\langle f, g \rangle = \int_0^{2\pi} f(\theta) g(\theta) \mathrm{d}\theta, \tag{6}$$

which results in the standard norm

$$\|f\| = \langle f, f \rangle^{1/2}, \tag{7}$$

the Proper Orthogonal Decomposition reduces to the problem of seeking functions $f_i(\theta)$, with f indicating wall pressure or wall shear stress, which are "most similar" in average to the snapshot ensemble.

It has been shown (7), that these functions are the eigenfunctions of the following integral eigenvalue problem

$$\int_0^{2\pi} \mathcal{R}^f(\theta,\theta^*) f(\theta^*) \mathrm{d}\theta^* = \lambda^f f(\theta) \tag{8}$$

where $\mathcal{R}^f$ is the two-point spatial correlation tensor associated to f given by

$$\mathcal{R}^f(\theta,\theta^*) = \frac{1}{T}\int_0^T f(t,\theta)\, f(t,\theta^*)\, \mathrm{d}t \tag{9}$$

The eigenvalues λ_i^f of (8) are all positive and define a convergent series. The POD basis functions are normalised such that $\|f_i(\theta)\| = 1$. The temporal coefficients $a_i^f(t)$ are then obtained by the projection of the i-th POD mode with the snapshots $a_i^f(t) = \langle f(t,\theta), f_i(\theta)\rangle$. By construction, the temporal coefficients form an orthogonal set, i.e. they satisfy the property

$$\frac{1}{T}\int_0^T a_i^f(t) a_j^f(t)\, \mathrm{d}t = \lambda_i^f \delta_{ij} \tag{10}$$

where δ_{ij} is the Kronecker delta. As a measure of the information content in the POD basis functions of the variable f, we introduce the relative information content (RIC), see e.g. (30), defined as

$$\mathrm{RIC}^f(n) = \sum_{i=1}^{n} \lambda_i^f \Big/ \sum_{i=1}^{N} \lambda_i^f . \tag{11}$$

3.2.1 Reduced order modelling by wall-based POD: results

In figure 5, the relative information content RIC(n) is reported for both the wall pressure and the wall shear stress fluctuations. Numerical values are also reported for reference in table 2. We observe that a very small number of basis functions are sufficient to describe with significant accuracy the energy of the fluctuations of the two flow variables at the wall. In particular, four spatial modes capture more than 99.9% of the total fluctuation energy for both the wall variables. As a result, in the rest of the paper we will consider only these eight basis functions for the representation of the variables. Interestingly, the spatial structure of the wall pressure appears slightly simpler than that of the shear stress, as more energy is captured for the same number of modes.

Similar data compression results are obtained for full-field decompositions, see for instance Bergmann et al. (30). This appears to indicate that all the large scale structures in the flow field have a strong impact on the fluctuations on the wall, as will be elucidated better later in the paper, in section 4. This fact is certainly not obvious a priori, and should not hold as a general rule, because the wall and full-field bases are optimal in two different senses. The full-field decomposition is biased to represent those regions of the flow field where fluctuations are more intense, while the dynamics in other regions of the flow field might have lesser representation in the POD basis, even though they might have strong dynamical importance, or they might have more fundamental interest, see e.g. Rowley (48). In contrast, for the wall-based modelling discussed here, the POD focuses on a very specific and localised region of the flow field, to represent optimally the wall fluctuations.

Polar plots of the first six spatial structures $\tau_i(\theta)$ identified by the POD analysis for the wall shear stress are reported in figure 6. For each distribution, the thin grey line represents the time averaged wall shear stress distribution $\tau_0(\theta)$, whereas the basis functions are represented wth a

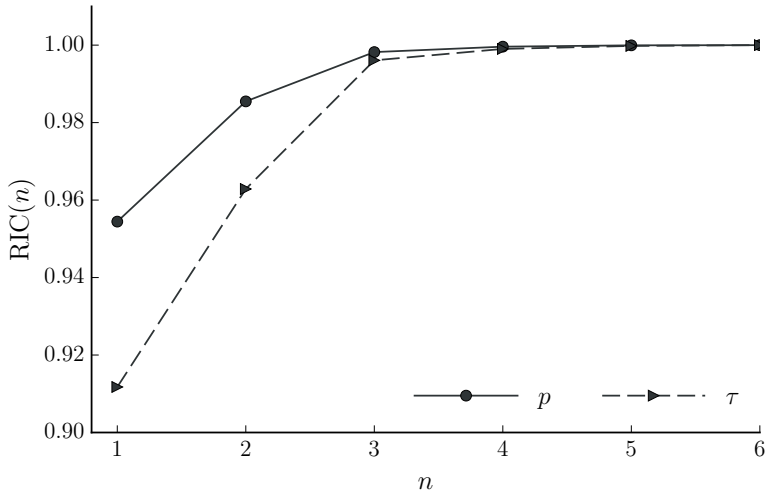

Figure 5: Relative information content for the Proper Orthogonal Decomposition of the wall pressure and wall shear stress fluctuations.

n	1	2	3	4
$\mathrm{RIC}^p(n)$	0.954	0.985	0.998	0.999
$\mathrm{RIC}^\tau(n)$	0.912	0.963	0.996	0.999

Table 2: Numerical values of the relative information content for the wall pressure and the wall shear stress decompositions as in figure 5, for the first four modes.

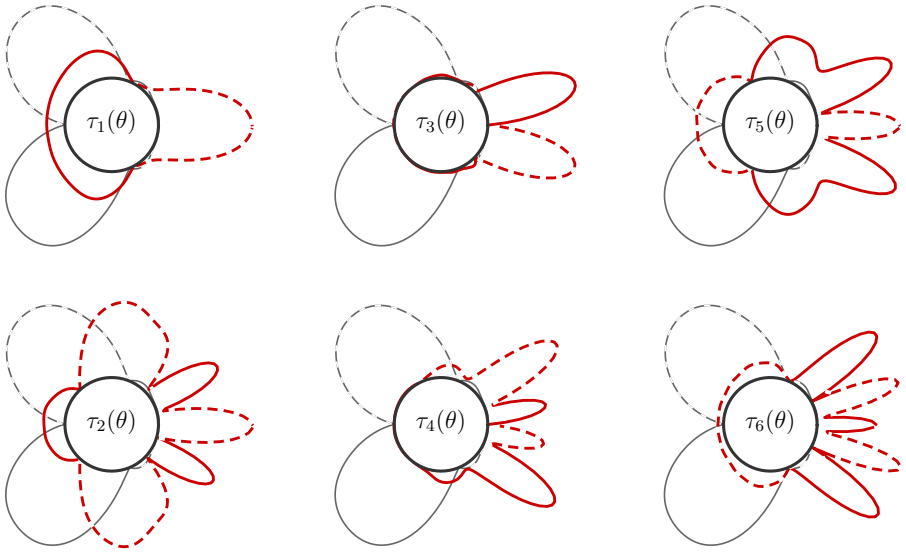

Figure 6: First six empirical modes identified by the POD analysis of the wall shear stress data, (thick red line). The thinner grey line represents the time averaged wall shear stress distribution. Negative values are represented by a dashed line.

thicker red line. For both, the dashed part denotes a negative value. For graphical purposes, the modes have been reported on an arbitrary radial scale, such that their maximum value equals the maximum value of the mean distribution in the background.

The basis functions display a high degree of symmetry, similarly to full-field pod modes (e.g. (26)). Modes that are symmetric with respect to $\theta = 0$, i.e. such that $\tau_i(\theta) = \tau_i(-\theta)$, modes 1, 2, 5, and 6, describe fluctuations of the viscous force in the vertical direction, i.e. of the lift. On the other hand, anti-symmetric modes, i.e. such that $\tau_i(\theta) = -\tau_i(-\theta)$, modes 3 and 4, describe fluctuations of the drag component. The first wall shear stress mode, which captures about 91% of the total fluctuation energy, describes a large scale fluctuation of the wall shear stress induced by the periodic "rotation" of the flow around the cylinder generated by the alternated reattachment of the separated shear layers over the upper and lower parts of the cylinder.

The other modes represent less energetic fluctuations of the wall shear stress in the rear part of the cylinder, in the region of separated flow. These basis functions capture the fluctuations of the shear stress induced at the wall by those small scale features, e.g. recirculation bubbles and shear layers detaching from the wall, that populate the rather active back region in close vicinity of the cylinder (37).

The first six wall pressure modes $p_i(\theta)$ identified by the POD are shown in figure 7. Similarly to the wall shear stress, these basis functions display a high degree of symmetry. For this case, anti-symmetric modes, (1, 2, 5 and 6), describe lift fluctuations whereas symmetric modes, 3 and 4, described drag fluctuations. The first pressure mode displays two large lobes of opposite sign, which describe the large scale fluctuations of lift induced by the shedding. Similarly, the second

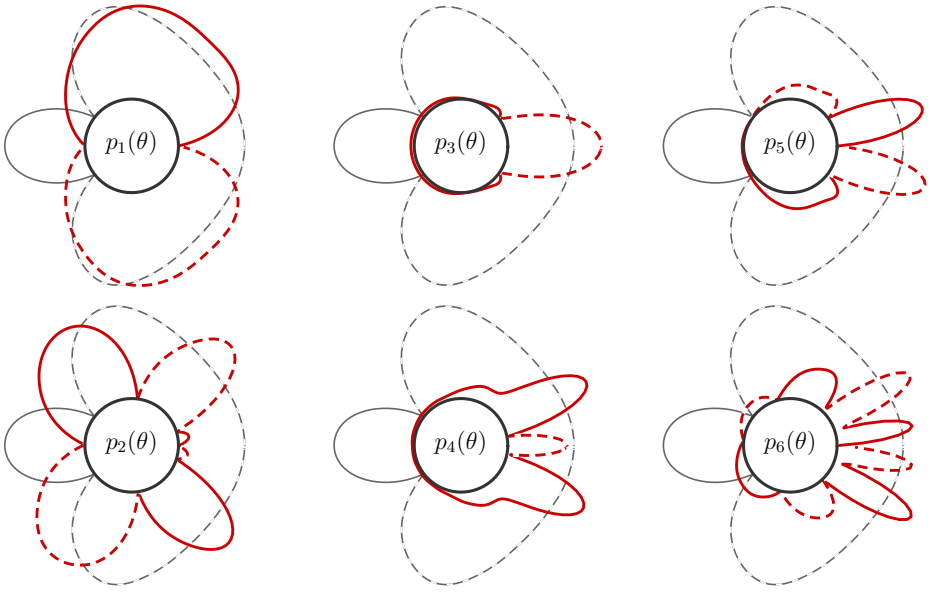

Figure 7: First six basis function identified by the POD analysis for the wall pressure, (thick red line). The thin grey line represents the time averaged wall pressure distribution. Negative values are indicated by a dashed line.

mode has a four-lobe structure. Together, these two modes account for a total of about 98% of the total energy of the wall pressure fluctuations. The fact that the two symmetric modes have a relatively small contribution to the total energy of the pressure fluctuation is related to the fact that the lift coefficient show much larger fluctuations than the drag coefficient.

The time histories of the measured temporal coefficients $a_i^\tau(t)$ and $a_i^p(t)$ of the first six wall shear stress and wall pressure basis functions are reported in the top and bottom panels, respectively, of figure 8. The panels show the temporal evolution of the pairs of modes (1, 2), (3, 4) and (5, 6). A notable feature, for both the pressure and the shear stress, is that the n-th pair of modes approximately defines an oscillation at the n-th harmonic of shedding frequency.

A similar property has been also observed for the full-field decomposition of the cylinder flow (25; 50; 26). The first pair of modes describes the fluctuations of the lift coefficient, while the second pair of modes the fluctuations of the drag, which oscillates at twice the fundamental frequency. The third pair also describes a lift fluctuation but at a higher harmonic of the shedding frequency.

3.3 Dynamic model for the wall shear stress

It is evident that there is no governing equation that determines the evolution of the shear stress at the wall because the Navier-Stokes equations refer to the evolution of the flow within the domain. As a result there is no dynamical equation that could be possibly used for the Galerkin projection to obtain a system of ordinary differential equation for the temporal coefficients of the wall pressure or the wall shear stress.

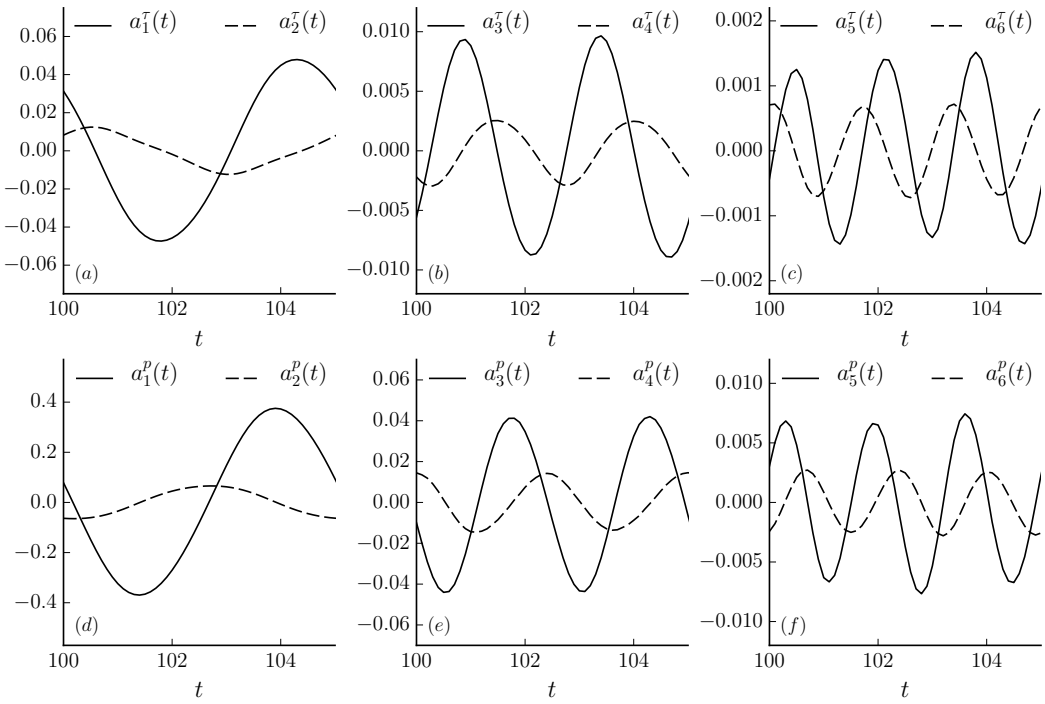

Figure 8: Time histories of the temporal coefficients for the first six basis functions of the wall shear stress, top three panels, and for the wall pressure, bottom panels.

The apparent difficulty can be overcome by using the Galerkin projection method for the vorticity form of the Navier-Stokes equations, which we outline for the case of a two-dimensional flow. An extension to the three-dimensional case is presented in appendix A. To provide an in depth basis on the projection for the vorticity equation, the classical work of Rempfer et al. (44) and the more recent work of Cordier et al. (5) can be consulted.

We assume that it is possible to represent, to an arbitrary degree of accuracy, the scalar vorticity field $\omega = \partial v/\partial x - \partial u/\partial y$ as a weighted sum of a set of vorticity basis functions $\{\omega_i(\boldsymbol{x})\}_{i=0}^{N_\omega}$, as

$$\omega(\boldsymbol{x}, t) \simeq \omega_0(\boldsymbol{x}) + \sum_{i=1}^{N_\omega} a_i^\omega(t)\omega_i(\boldsymbol{x}) \tag{12}$$

where $\omega_0(\boldsymbol{x})$ is the time-averaged field, hence $a_0^\omega(t) = 1$ for all times. There is no requirement for how the vorticity basis functions are derived, except for the constraint that the associated velocity fields $\{\boldsymbol{u}_i\}_{i=0}^{N_\omega}$ must be solenoidal and must satisfy the boundary conditions of the original problem in the velocity-pressure formulation. The Galerkin projection of the vorticity transport equation

$$\frac{\partial \omega}{\partial t} = -\boldsymbol{u} \cdot \nabla\omega + \frac{1}{Re}\nabla^2\omega, \tag{13}$$

onto each vorticity basis function yields a system of ordinary differential equations of the form

$$\sum_{j=1}^{N^\omega} M_{ij}\frac{\mathrm{d}a_j^\omega}{\mathrm{d}t} = \sum_{j=0}^{N^\omega} L_{ij}a_j^\omega + \sum_{j=0}^{N^\omega}\sum_{k=0}^{N^\omega} N_{ijk}a_j^\omega a_k^\omega \quad \text{for } i = 1, \ldots, N^\omega, \tag{14}$$

where the tensors M_{ij}, L_{ij} and N_{ijk} are defined by integrals over the flow domain Ω as

$$M_{ij} = \int_\Omega \omega_i\omega_j \mathrm{d}\Omega, \quad L_{ij} = \frac{1}{Re}\int_\Omega \omega_i\nabla^2\omega_j \mathrm{d}\Omega, \quad N_{ijk} = -\int_\Omega \omega_i(\boldsymbol{u}_j \cdot \nabla)\omega_k \mathrm{d}\Omega. \tag{15}$$

Specification of appropriate initial conditions and time integration of the system (45) provides a reduced order solution of the vorticity field by equation (12). This approach is fairly standard and general properties of these systems are well-known.

Now, because the vorticity fields $\omega_i(\boldsymbol{x})$ are global modes defined on the entire domain, it can be argued that the time evolution of the vorticity along some curve in the domain parametrised by the coordinate η is given by the weighted sum of the vorticity basis functions evaluated on the curve and where the weights are just the temporal coefficient solution of (45) i.e.

$$\omega(\eta, t) = \omega_0(\eta) + \sum_{i=1}^{N_\omega} a_i^\omega(t)\omega_i(\eta). \tag{16}$$

If that curve is a wall, the wall shear stress can be easily obtained from the vorticity as $\tau(\eta, t) = \omega(\eta, t)/Re$. As a result, the temporal evolution of the shear stress on the surface is also given by

$$\tau(\eta, t) = \tau_0(\eta) + \sum_{i=1}^{N_\omega} a_i^\omega(t)\tau_i(\eta) \tag{17}$$

where $\tau_i(\eta)$ is the wall shear stress associated to the vorticity mode $\omega_i(\boldsymbol{x})$ evaluated on the curve. By comparing equations (12) and (51), it can be argued that the system (45) also describes the

evolution of the temporal coefficients associated with the wall basis functions $\{\tau_i(\eta)\}_{i=0}^{N_\omega}$. Thus, any solution of (45) provides the required spatio-temporal description of the wall shear stress.

A necessary relaxation, then, comes from the fact that (12) does not impose any particular constraint on the choice of the vorticity basis functions. As a result, one can take the reverse direction and choose the wall basis functions $\{\tau_i(\eta)\}_{i=0}^{N_\omega}$ as it is more convenient, for example such that these wall functions are optimal to represent the energy of the fluctuations at the wall, as it has been discussed in section 3.2.

3.4 Identification of the shear stress dynamic model

For an arbitrary choice of the set of $\{\tau_i(\eta)\}_{i=0}^{N_\omega}$, one would need to have handy the associated vorticity basis functions on the rest of the domain. If these are available, numerical evaluation of the integrals in (46) specifies the set of coefficients M_{ij}, L_{ij} and N_{ijk}.

However, within the framework of the wall-based modelling addressed in this paper, we assume that only the signature at the wall of the vorticity basis functions, i.e. measurements of the wall shear stress, is available. Hence, it is not possible to adopt the projection method to derive the coefficients of the low order model. The difficulty can be circumvented by assuming that the same set of unknown coefficients in (45) can be identified from raw wall measurements, an approach which we pursue in this work.

In the context of low order modelling for fluids, model calibration methods to correct the dynamic behaviour have been discussed extensively. In the identification method discussed in (51; 46; 52), the system parameters are obtained by fitting, in the least squares sense, the time derivatives of the temporal coefficients to the quadratic structure of the right hand side of the state equation. The resulting system of linear equations is structurally very ill-conditioned and severely affects the result. More robust solution methods, based on a truncated singular value decomposition of using other regularisation approaches, have to be used for the numerical solution, (52). However, based on extensive tests of this approach on the present dataset, we have found that the systems identified with this method are extremely unstable when they are integrated in time, and the instability worsens for models with a high number of modes, quickly exhibiting numerical blow-up, similarly to the behaviour discussed by Cordier et al., (52).

Hence, to cope with this issue we have used a system identification scheme that ensures a more accurate representation of the long-term behaviour of the ROM. We follow the approach reported in reference (52) and references therein. For convenience, the system in equation (45) is rewritten in a form that is more suited for identification. This form is given by

$$\frac{\mathrm{d}\tilde{a}_i^\tau}{\mathrm{d}t} = A_i + \sum_{j=1}^{N_\tau} B_{ij}\tilde{a}_j^\tau + \sum_{j=1}^{N_\tau}\sum_{k=j}^{N_\tau} C_{ijk}\tilde{a}_j^\tau\tilde{a}_k^\tau \quad \text{for } i = 1,\ldots,N_\tau, \tag{18}$$

where the sums start from $j = 1$, and the interaction with the mean mode is given by the constants A_i. All the coefficients A_i, B_{ij} and C_{ijk} have to be identified. Note that a compact form is used for the double summation in nonlinear term, so that the pairs of quadratic monomials with $j \neq k$ are considered only once. The tilde indicates the model prediction as opposed to the analogous measured quantities obtained by POD. A more compact form can be given as

$$\frac{\mathrm{d}\tilde{\boldsymbol{a}}^\tau}{\mathrm{d}t} = \boldsymbol{f}(\tilde{\mathbf{a}}^\tau(t);\Theta) \tag{19}$$

where $\tilde{\boldsymbol{a}}^\tau(t) \in \mathbb{R}^{N_\tau}$ is the state vector containing the predictions of the temporal coefficients. The vector function $\boldsymbol{f} : \mathbb{R}^{N_\tau} \to \mathbb{R}^{N_\tau}$ wraps the sums in (18) and it is parametrised by the matrix

$$\Theta = [\boldsymbol{\theta}_1, \ldots, \boldsymbol{\theta}_i, \ldots, \boldsymbol{\theta}_{N_\tau}] \in \mathbb{R}^{N_m \times N_\tau} \tag{20}$$

where each column $\boldsymbol{\theta}_i \in \mathbb{R}^{N_m}$ lists the N_m coefficients for the i-th state equation in (18), i.e.

$$\boldsymbol{\theta}_i = [A_i | \, B_{i1} \ldots B_{iN_\tau} | \, C_{i11} \, C_{i12} \ldots C_{i1N_\tau} \, C_{i22} \ldots C_{i2N_\tau} \ldots C_{iN_\tau N_\tau}] \in \mathbb{R}^{N_m} \tag{21}$$

The initial conditions for (19) are taken from the measured values, that is $\tilde{\boldsymbol{a}}(t_0) = \boldsymbol{a}(t_0)$ for some t_0. The dimension N_m is the number of unique monomials for a quadratic polynomial in N_τ variables, which is equal to $1 + N_\tau + N_\tau(N_\tau + 1)/2$.

The system identification problem consists in finding a model whose predictions are closest, in average and in some norm, to the analogous measured quantities. Hence, we first define the instantaneous error vector $\boldsymbol{e}(t) = \boldsymbol{a}^\tau(t) - \tilde{\boldsymbol{a}}^\tau(t) \in \mathbb{R}^{N_\tau}$ and the symmetric positive definite matrix $\Lambda \in \mathbb{R}^{N_\tau \times N_\tau}$ that induces the norm $\|\boldsymbol{e}(t)\|^2_\Lambda = \boldsymbol{e}(t)^T \Lambda \boldsymbol{e}(t)$. We thus seek the matrix of coefficients Θ^o that minimises the cost

$$\mathcal{J}(\Theta; T) = \frac{1}{T} \int_0^T \|\boldsymbol{e}(t)\|^2_\Lambda \, \mathrm{d}t \tag{22}$$

subject to the state equation (19). In the present case we used a diagonal structure for Λ with entries $\Lambda^{-1}_{ii} = 1/T \int_0^T a_i^\tau(t)^2 \mathrm{d}t$ to weight each state according to its relative mean energy content. This improves the conditioning of the problem and speeds up the optimisation.

Besides the difficulty of the solution of this optimisation problem due to the large number of parameters, a further and principal issue stems from the non-convexity of this class of optimisation problems, which are usually plagued by the presence of many local optima, (46). Hence, in order to relax this complexity we adopted an iterative approach where the integration horizon T in (22) is increased gradually to include first a few data points and eventually the complete data set. When the time horizon is increased, the optimisation problem is restarted from the optimal solution found at the previous iteration. At first, $\Theta = 0$. This approach results in a sequence of better behaved optimisation problems, each of which started from a solution which is already close to the global minimum at the current iteration. Although this procedure is not guaranteed to converge in the most general case, it worked satisfactorily on the present dataset. An interesting alternative is the so-called multiple-shooting method, (53), where time integration of the system is performed from several initial conditions and the sum of the errors over all the blocks of data is taken as the performance index to be minimised.

In the present case, $N_\tau = 4$, with a total of 60 parameters to estimate. We used with success the Broyden-Fletcher-Goldfarb-Shanno (BFGS) algorithm to solve the optimisation problems at each outer iteration. We have found that the time horizon had to be increased quite finely during the first iterations covering the first shedding cycle, in order to prevent instabilities.

In figure 9 the time histories of the optimised model predictions $\tilde{a}_i^\tau(t)$ are compared to analogous measured quantities $a_i^\tau(t)$. The match between the model predictions and the full-order system data is good. A major source of error, especially for the first state, is a frequency component at four times the shedding frequency, which disappears when identifying a model with six states, instead of four. For clarity the figure shows only the first two shedding cycles, but the resulting model is quite stable and does not show drifts or instabilities over the time span of the data from which it was identified, i.e. for about 200 time units.

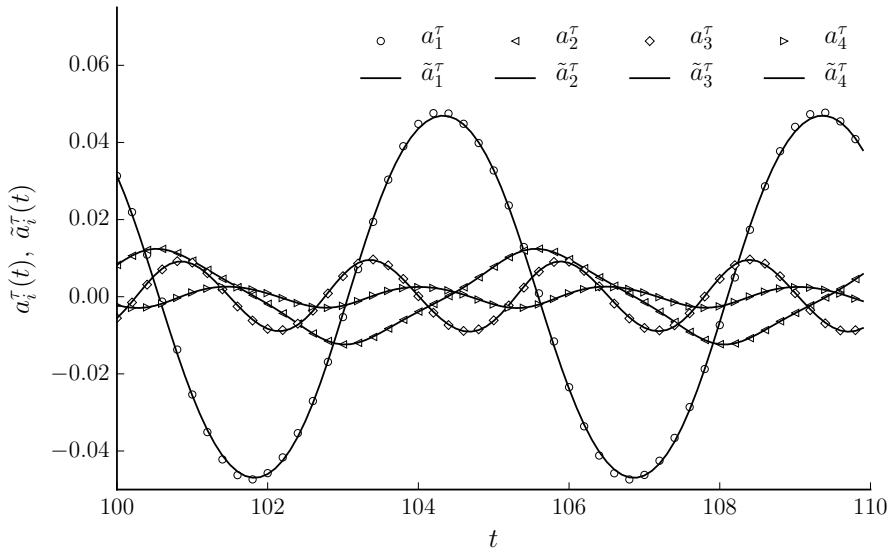

Figure 9: Comparison between the measured and predicted time histories of the temporal coefficients of the wall shear stress basis functions.

There is one important remark that needs to be included in this discussion. In the most general case, the wall shear stress distribution does not uniquely determine its future evolution. This occurs because there might exist more than one vorticity field distribution, hence with different temporal evolution given by (44), with the same identical wall distribution of shear stress. This might be the case where the motion of coherent structures decouples from their signature on the wall, for more complex flows, or when the flow is actuated. Such events would likely affect the model identification stage discussed here, resulting in a less accurate model.

3.5 Estimation of the wall pressure distribution

For flows around bluff bodies, and generally for separated flows at large Reynolds number, the wall pressure distribution determines the forces acting on the body itself, whereas the viscous contribution is often negligible. However, since the dynamic model derived in the previous section only contains the wall shear stress, a method that allows an accurate estimation of the wall pressure distribution from the wall shear stress is needed.

We start with the ansatz that the vorticity field equals the weighted sum of a finite number of vorticity basis functions,

$$\omega(\boldsymbol{x},t) = \sum_{i=0}^{N_\omega} a_i^\omega(t)\omega_i(\boldsymbol{x}) \tag{23}$$

The sum includes the mean vorticity field $\omega_0(\boldsymbol{x})$, with the corresponding weight $a_0^\tau(t) = 1$ being constant over time. The velocity field is then readily obtained upon use of the Biot-Savart law (54),

$$\boldsymbol{v}(\boldsymbol{x},t) = \frac{1}{2\pi}\int_\Omega \boldsymbol{K}(\boldsymbol{x}-\boldsymbol{y})\omega(\boldsymbol{y})\,\mathrm{d}\Omega \tag{24}$$

where the vector kernel $\boldsymbol{K}(\boldsymbol{z})$ is defined as

$$\boldsymbol{K}(\boldsymbol{z}) = \Big(-\frac{z_2}{|\boldsymbol{z}|^2}, \frac{z_1}{|\boldsymbol{z}|^2} \Big) \tag{25}$$

Plugging the ansatz (23) into equation (24) the velocity field is then obtained as

$$\boldsymbol{v}(\boldsymbol{x}, t) = \sum_{i=0}^{N_\omega} a_i^\omega(t) \boldsymbol{u}_i(\boldsymbol{x}) \tag{26}$$

where the basis functions $\boldsymbol{u}_i(\boldsymbol{x})$ are derived for each of the vorticity global modes from (24) as

$$\boldsymbol{u}_i(\boldsymbol{x}) = \frac{1}{2\pi} \int_\Omega \boldsymbol{K}(\boldsymbol{x} - \boldsymbol{y}) \omega_i(\boldsymbol{y}) \, \mathrm{d}\Omega \tag{27}$$

Obtaining the pressure field, and thus the pressure on the surface, would require the solution of a Poisson equation. To this end, we follow the approach and some of the notation introduced by Noack et al. (24). The pressure Poisson equation is derived by taking the divergence of the Navier-Stokes equations (1). For a two-dimensional flow it is given by

$$\Delta p = -\sum_{l=1}^{2} \sum_{m=1}^{2} \frac{\partial v^m}{\partial x^l} \frac{\partial v^l}{\partial x^m} = s. \tag{28}$$

In this equation, the superscripts l and m run over the Cartesian components of the vectors $\boldsymbol{v}$ and $\boldsymbol{x}$. To reduce clutter in the notation, the source term at the right hand side of the Poisson equation will be denoted by s. We assume that an appropriate choice of the boundary condition for the solution of equation (28) is made. This is actually not required, since the Poisson equation needs not to be solved. With the ansatz of equation (26), the source term s in (28) reads as a quadratic functional of the temporal coefficients a_i^ω

$$s = \sum_{i=0}^{N_\omega} \sum_{j=0}^{N_\omega} s_{ij} a_i^\omega a_j^\omega \tag{29}$$

where the quantities s_{ij} are defined for each pair of modes

$$s_{ij} = -\sum_{l=1}^{2} \sum_{m=1}^{2} \frac{\partial u_i^m}{\partial x^l} \frac{\partial u_j^l}{\partial x^m}, \tag{30}$$

where the subscripts denote the mode number as in the rest of the paper. As a result, the solution of the Poisson equation (28) can be expressed as

$$p(\boldsymbol{x}, t) = \sum_{i=0}^{N_\omega} \sum_{j=0}^{N_\omega} \mathrm{p}_{ij}(\boldsymbol{x}) a_i^\omega(t) a_j^\omega(t) \tag{31}$$

where each of the partial pressures p_{ij} fields satisfies its own Poisson equation $\Delta \mathrm{p}_{ij} = s_{ij}$.

Equation (31) states that the pressure field can be obtained as a weighted sum of partial pressure fields, derived from the vorticity modes, with weights quadratic in their amplitudes. On the surface of the cylinder, equation (31) results in

$$p(\theta,t) = \sum_{i=0}^{N_\omega}\sum_{j=0}^{N_\omega} \mathrm{p}_{ij}(\theta) a_i^\omega(t) a_j^\omega(t). \tag{32}$$

whereas, within the reduced order modelling framework discussed here, the same quantity is expressed by the expansion in (5). This results in the equality

$$\sum_{l=0}^{N_p} a_l^p(t) p_l(\theta) = \sum_{i=0}^{N_\tau}\sum_{j=0}^{N_\tau} \mathrm{p}_{ij}(\theta) a_i^\tau(t) a_j^\tau(t) \tag{33}$$

where we have changed the superscript from ω to τ, because of the fundamental equivalence of the two quantities. This equation closely relates the unknown temporal coefficients $a_l^p(t)$ with the known temporal coefficients $a_i^\tau(t)$. To obtain an explicit relation we multiply both sides by each of the wall pressure basis function $p_k(\theta)$ in turn and we integrate along the cylinder body. The mutual orthogonality property of the wall pressure basis functions obtained via the POD of the surface data leads to the final expression

$$a_l^p(t) = \sum_{i=0}^{N_\tau}\sum_{j=0}^{N_\tau} w_{lij} a_i^\tau(t) a_j^\tau(t), \quad l = 1,\ldots,N^p, \tag{34}$$

where $w_{lij} = \langle p_l(\theta), \mathrm{p}_{ij}(\theta)\rangle$. Note that $a_0^p(t) = 1$ by construction and does not need to be estimated.

Equation (34) states that at any time it is possible to determine the fluctuating pressure field on the surface from measurements of the wall shear stress. In principle, numerical values of the weights w_{lij} could be rigorously derived from the solution of the partial pressures Poisson equations, with appropriate boundary conditions. However, this approach would require the full-field vorticity modes $\omega_i(\boldsymbol{x})$ to be available, whereas within the proposed technique only their values at the wall, i.e. the wall shear stress distribution is available. For this reason, we propose that a more direct way to derive these weights is to use a least-square fitting approach using the temporal coefficients obtained from POD. Because the least squares problem is ill-conditioned we have adopted a solution based on truncation of the singular value decomposition, see references (51; 52; 55) for details. Using time histories of $a_i^p(t)$ and $a_i^\tau(t)$, the convex optimisation problem amounts to finding the optimal set of coefficients w_{lij} that minimises the cost

$$E_l^2(w_{lij}) = \int_0^T \left[a_l^p(t) - \sum_{i=0}^{N_\tau}\sum_{j=0}^{N_\tau} w_{lij} a_i^\tau(t) a_j^\tau(t)\right]^2 \mathrm{d}t \tag{35}$$

for each $l = 1,\ldots,N_p$ separately.

Despite the fact that the structure (34) is quadratic, linear terms are still included since the mean mode amplitude $a_0^\tau(t)$ is equal to one, and thus the cross terms resulting from the interaction with the mean mode are such that $a_0^\tau a_i^\tau = a_i^\tau$. It is thus important to understand if the inclusion of the quadratic terms significantly improves the estimate, with respect to a linear expansion of the form

$$a_l^p(t) = \sum_{i=1}^{N_\tau} v_{li} a_i^\tau(t), \quad l = 1,\ldots,N^p, \tag{36}$$

	ϵ_1	ϵ_2	ϵ_3	ϵ_4
linear	0.035	0.093	0.056	0.060
quadratic	0.000	0.000	0.002	0.010

Table 3: Normalised root-mean-square error in the estimation of the wall pressure temporal coefficients from the wall shear stress temporal coefficients, based on linear or quadratic expansion.

where optimal weights v_{li}^o can be obtained similarly to the quadratic case by solution of an analogous linear least squares problem. This observation relates to the development of linear models of the pressure gradient term in the Galerkin projection for full-field decompositions, as discussed by Galletti (23). To quantify the accuracy of the estimation we report in table 3 the normalised root-mean-square error

$$\epsilon_l = \sqrt{E_l^2 / \int_0^T a_l^p(t)^2 \mathrm{d}t} \tag{37}$$

computed for the four-mode model for both the linear and the quadratic expansions. It is clear that the linear expansion (36) already provides a very accurate description of the wall pressure distribution. The addition of the quadratic term does not change substantially the results.

This result is evident by observing the time histories of the measured $a_i^p(t)$, and predicted, $\tilde{a}_i^p(t)$, wall pressure temporal coefficients, reported in figure 10, for the first and the last wall pressure temporal coefficients, in the left and right panels, respectively. It can be observed that the match between the predictions and the measured values is actually quite good.

A fundamental explanation for why the linear expansion already works remarkably well lies in the fact that the spectral content of the wall pressure and the wall shear stress temporal coefficients is very similar between pairs of modes. In fact, as discussed in figure 8, the i-th pair of modes describes fluctuations at the i-the harmonic of the shedding frequency, for both the wall pressure and the wall shear stress. As a result, to estimate the first wall pressure mode $a_1^p(t)$ it is sufficient to use a linear combination of the first two shear stress modes $a_1^\tau(t)$ and $a_2^\tau(t)$, to recover the right phase difference, since these two are orthogonal to each other and basically represent sine/cosine functions oscillating at the shedding frequency. The third and fourth shear stress modes have a limited effect on $a_1^p(t)$ because the energy at twice the shedding frequency is relatively small in $a_1^p(t)$. A similar argument can be introduced for the other modes.

The need for a quadratic term arises when the spectral content of the a_i^τ is not sufficient to match the spectral content of some of the a_l^p in a linear sense. This would be the case when the spectral content of the temporal coefficients is more complex and a lesser separation of frequency components is found. For instance, building a model with three modes only, e.g. eliminating mode 4 from the current model, results in the fact that mode a_3^p cannot be accurately determined using only mode a_3^τ because there is a phase difference between the two, (compare panels b and e of figure 8). As a result a quadratic term containing modes with lower frequency is required to generate components at twice the shedding frequency, to match the right phase of a_3^p.

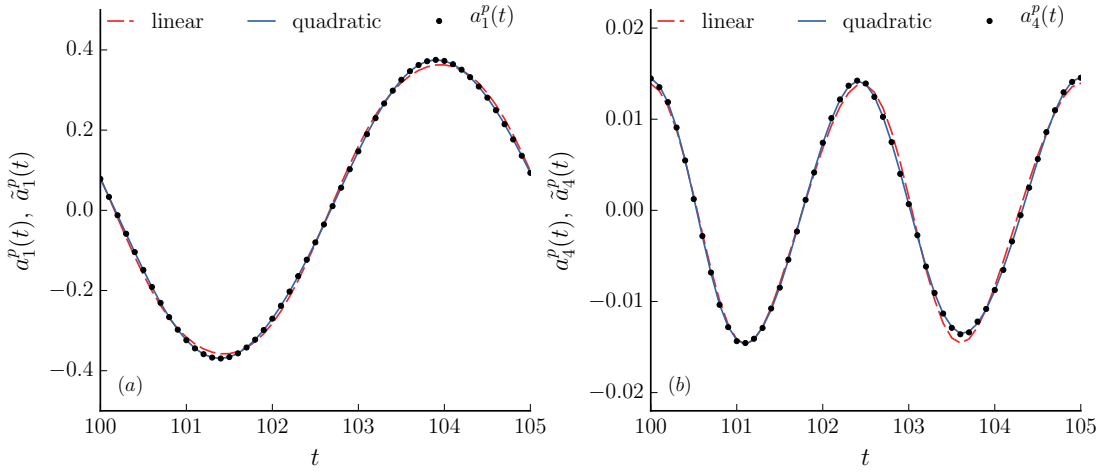

Figure 10: Time histories of the measured and estimated temporal coefficients of the wall pressure basis function $p_1(\theta)$ and $p_4(\theta)$. Results for both linear and quadratic formulations are displayed.

3.6 Lift, drag and separation point predictions

The drag and lift forces can be computed as linear combinations of the temporal coefficients as

$$C_D(t) = \sum_{i=0}^{N_\tau} C_{Di}^\tau a_i^\tau(t) + \sum_{i=0}^{N_p} C_{Di}^p a_i^p(t) \tag{38a}$$

$$C_L(t) = \sum_{i=0}^{N_\tau} C_{Li}^\tau a_i^\tau(t) + \sum_{i=0}^{N_p} C_{Li}^p a_i^p(t) \tag{38b}$$

where the coefficients C_{Di}^τ, C_{Di}^p and C_{Li}^τ, C_{Li}^p are the viscous and pressure contributions to the drag and lift coefficients, respectively, and are computed for each wall shear stress and wall pressure basis function in (5) with equations (3) and (4). This aspect would be certainly advantageous in cases where control of the flow over aerodynamic bodies is of interest, although it is beyond the scope of this paper to discuss this aspect. It can be argued that the wall-based formulation provides a straightforward and accurate way to express the aerodynamic forces as a function of the system state, thus avoiding the need to define arbitrary "drag-related" cost functions of states representing full-field modes (56; 30).

In figure 11 we report time histories of the predicted lift, panel (a), and drag coefficients, panel (b), compared to the same quantities measured from direct numerical simulations. We observe that the predictions are in very good agreement with the measured data. This is particularly true for the lift coefficient, which accounts for the largest contribution to the forces, while a slight difference can be detected for the drag, essentially because of the early truncation of the basis. For a model based on six modes, we have observed that the measured and predicted time histories are indistinguishable from the plot. This is because the basis functions were derived by POD and the wall pressure fluctuations are distributed such that the fluctuations in the vertical direction are

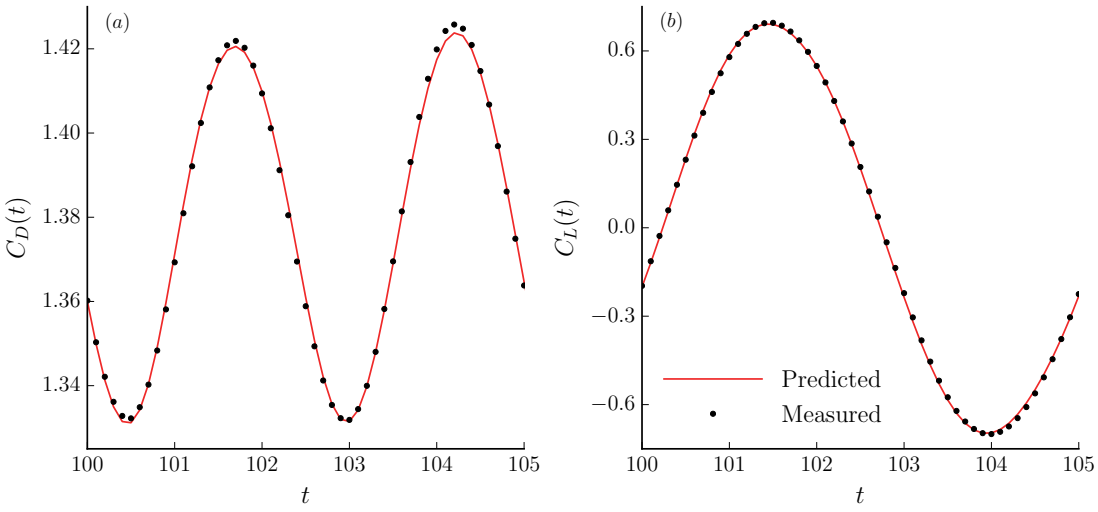

Figure 11: Time histories of the measured and predicted drag, (a), and lift, (b), coefficients.

dominant with respect to those along the free stream direction. In particular, only modes $p_3(\theta)$ and $p_4(\theta)$ describe fluctuations that contribute to the drag while all the other four describe the lift fluctuations.

The force coefficients are integral quantities from which the prediction accuracy of the model can be assessed only globally. In spite of this, the model derived with the proposed approach also allows a very accurate description of the flow features on the wall. Such knowledge might be advantageous in certain situations. One example, that we investigate in this case, is the time-dependent separation location $\theta_{sep}(t)$, intended in the current case as the angle where the wall shear stress vanishes.

In figure 12 we report time histories of the measured and predicted separation location. The predictions of the model is obtained by first reconstructing the surface shear stress distribution from the predicted temporal coefficients $\tilde{a}_i^{\tau}(t)$ of the four-mode model and from the basis functions $\tau_i(\theta)$ with equation (5) and then seeking in the expected region of separation the angle where the shear stress changes sign. Note that the mean shear stress distribution $\tau_0(\theta)$ is also used in the reconstruction. The separation location fluctuates with time in reason of the periodic shedding of vorticity from the cylinder. However, a relatively accurate prediction of the separation location, well within one degree, can be obtained by the wall-based model.

4 Comparison with full-field POD analysis

The wall-based modelling technique described in this paper focuses on providing a low-dimensional description of the forces acting on the cylinder body, which are due to the dynamics of the large scale structures. However, to obtain a reliable and physically sound model, it is important to understand in deeper detail the relation between the coherent structures in the flow field and the surface distributions of the pressure and the shear stress.

In figure 13 the colour map of the mean square value of the vorticity fluctuations $\xi(\boldsymbol{x})$, defined

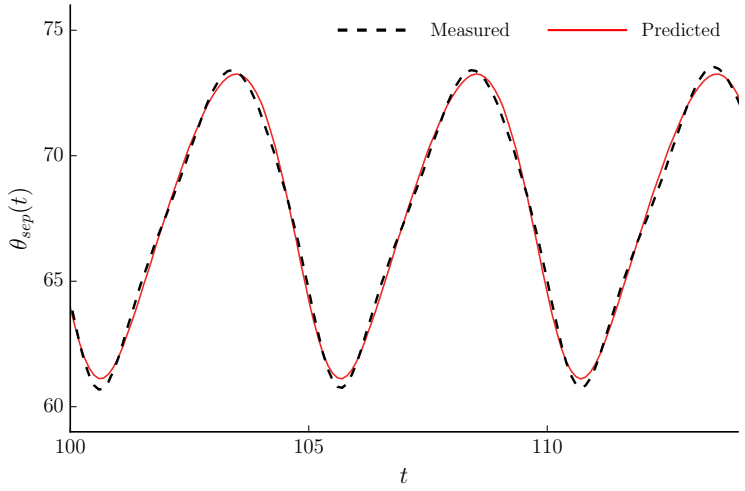

Figure 12: Measured and predicted separation point on the upper cylinder surface. Predictions are obtained from a calibrated model with $N_\tau = 4$.

as

$$\xi(\boldsymbol{x}) = \frac{1}{T}\int_0^T \omega^2(\boldsymbol{x}, t)\mathrm{d}t. \tag{39}$$

The colour scale is truncated at $\xi = 14$ for illustration purposes, even though maximum values of about 36 are reached in the rear region of the cylinder, where the intense fluctuations are due to the generation and growth of vortical structures. This is the area of the cylinder surface where the largest fluctuations of the wall shear stress are observed, and which are described by the wall shear stress basis functions, see figure 3-(a). However, the spatial distribution of ξ also displays a relatively large area in the near-wake region behind the cylinder, peaking at around 0.9 diameters behind the rear point, where fluctuations are much larger than those measured over most of the cylinder surface. In addition, the entire wake flow is subject to intense vorticity fluctuations, due to the periodic shedding and convection of vortices of alternating sign from the cylinder. As a result when POD is applied to the full-field dataset, the resulting basis functions may be biased by these fluctuations in the near- and far-field regions of the flow.

To identify a ranked set of full-field basis functions that optimally describe the large scale vortex dynamics in the near- and far-field regions of the cylinder, we used the snapshot variant (49) of the Proper Orthogonal Decomposition. The POD is applied to the fluctuating component of the vorticity dataset, based on 300 snapshot covering around 6 shedding cycles, to obtain the orthonormal set $\{\omega_j(\boldsymbol{x})\}_{j=1}^{N_\omega}$. It is worth noticing that the full-field basis functions have unit norm in the sense given by the norm

$$\|\omega_j(\boldsymbol{x})\| = \sqrt{\int_\Omega \omega_j^2(\boldsymbol{x})\,\mathrm{d}\Omega} \tag{40}$$

and thus their signature at the wall $\omega_j(\theta)$ does not have unit norm in the sense given by (7). In figure 14 colour maps of the spatial distribution of the first six full-field POD vorticity modes $\omega_j(\boldsymbol{x})$

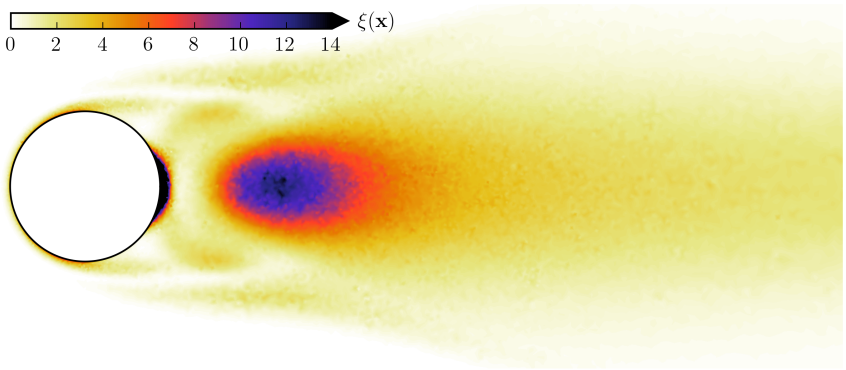

Figure 13: Colour map of the mean square value of the vorticity fluctuations $\xi(\boldsymbol{x})$ in the near-wake.

n	1	2	3	4	5	6
$\mathrm{RIC}^{\omega}(n)$	0.514	0.850	0.888	0.919	0.948	0.977

Table 4: Numerical values of the relative information content for the Proper Orthogonal Decomposition of the vorticity field, for the first six modes.

are shown. The plots show that the full-field basis functions target fluctuations in the wake region. Similarly to the shear stress wall functions, vorticity modes display a strong symmetry with respect to the axis $y = 0$. Interestingly, only the first four modes have a clearly visible signature on the cylinder surface, and thus influence the wall shear stress directly. High-order modes, which are commonly attributed to small-scale dissipative flow features, have very little support at the wall, and define vorticity fluctuations in the far-wake. This observation is related to the fact that the number of full-field POD basis functions required to recover a given fraction of fluctuation energy is different, and in particular larger that the analogous number required to describe the fluctuation energy at the wall. Analysis of the relative information content, as defined in equation (11), and reported in table 4 for the full-field vorticity POD analysis indicates that at least three times the number of full-field vorticity basis functions is necessary to achieve the same energy recovery at the wall obtained from 4 wall-modes. This is a clear indication of the strong reduction of dimensionality operated by considering fluctuations at the wall only, because all the flow structures that have no signature on it are intrinsically discarded.

In order to understand in a more quantitative manner the relationship between the full-field POD modes analysis and those obtained with the wall-based POD we calculate the unnormalised projection-like quantity

$$P_{ij} = \int_0^{2\pi} \tau_i(\theta)\omega_j(\theta)\,\mathrm{d}\theta \tag{41}$$

as a metric that quantifies the similarity between the i-th wall shear stress basis function $\tau_i(\theta)$ and the j-th full-field POD vorticity mode $\omega_i(\boldsymbol{x})$ evaluated at the wall. Strictly speaking, the physical dimensions of the two terms in the integral are different, but they are related to each other by the Reynolds number.

In figure 15 the distribution of the entries of P is illustrated for the first six wall shear stress

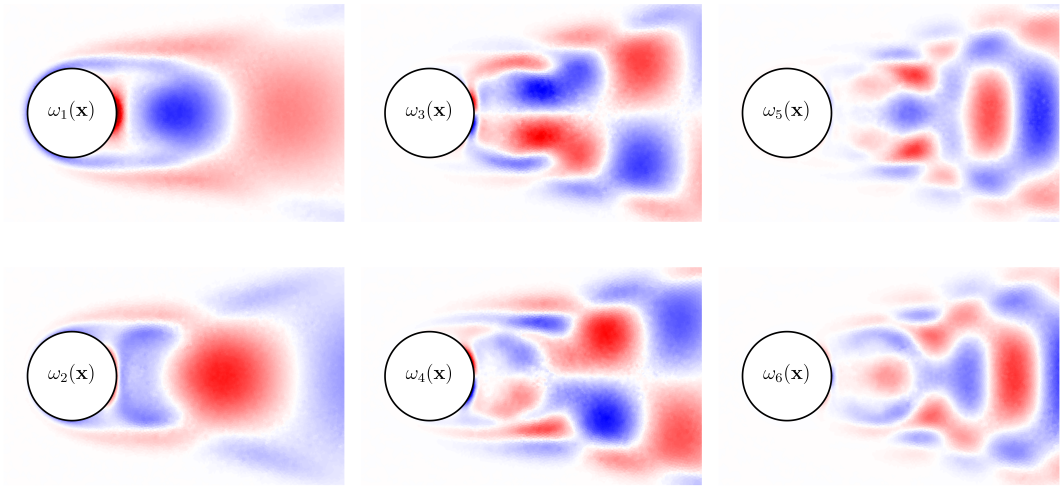

Figure 14: Colour maps of the first six full-field vorticity POD modes, reported over an arbitrary colour scale. Blue negative, red positive.

basis function and for the first six full-field vorticity modes. The quantity P has been rescaled for illustrative purposes by dividing it by its maximum absolute value. It can be seen that the matrix P has a relatively strong block diagonal structure up to $i, j = 4$, indicating that there is a relatively close relation between pairs field vorticity modes of figure 14 and pairs of wall shear stress modes in figure 6. This is due to the fact that the wall and field modes 1 and 2 describe lift fluctuations, while modes 3 and 4 described drag fluctuation. The result is a clear indication that the dynamics of the energy-relevant, large scale structures in the cylinder wake are taken into account by the wall-based model, as they have a relatively strong signature on the wall. However, the entries of P become increasingly smaller for $i, j > 4$, and the diagonal structure also starts to weaken. This feature confirms the qualitative discussion made for figure 14. In particular, the small-scale dissipative modes do not have in average a strong signature on the wall, and thus, they do not influence directly the aerodynamic forces, even though they influence the large scale dynamics via nonlinear inter-modal energy transfer. Hence, it can be argued that, in this case, the boundary $i, j = 4$ defines conceptually a separation between coherent structures that influence the unsteady loads on the cylinder and flow features that do not.

The role of the projection matrix P can be also viewed from a more generic system-theory-related standpoint. In general, for low order models constructed from the full-field data, the problem of estimating the state of the system from wall measurement arises, resulting in techniques as the Linear Stochastic Estimation, see Bonnet et al. (57) and references therein, and its variants, (58; 16; 59; 60), or in more rigorous methods for nonlinear dynamic systems (61; 62). From this standpoint, the quantity P_{ij} can be understood as an output equation that relates the observed outputs of the system a_i^τ, (which are, fundamentally, appropriate linear combinations of the sensor

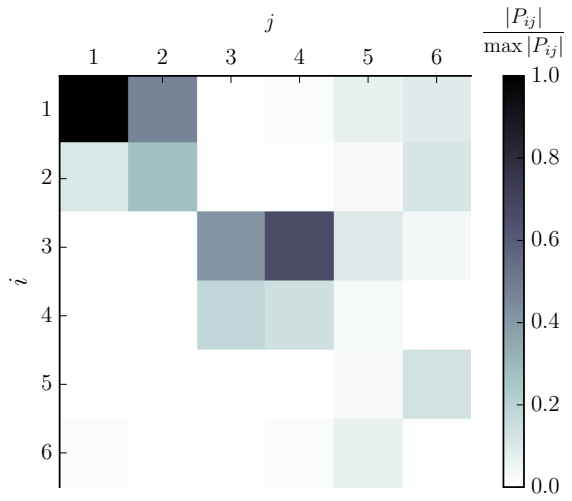

Figure 15: Absolute values of the normalised projection matrix P_{ij} of equation (41).

readings), to the internal states a_j^ω. This output equation would simply read as

$$a_i^\tau(t) = \sum_{j=1}^{N_\omega} P_{ij} a_j^\omega(t). \tag{42}$$

Even though the concept of observability of a dynamical system is more complex than what is briefly discussed here, it helps to build a conceptual model of the problem to see that if the matrix P is rank deficient, as it turns out to be in this case if i and j are large enough, some states a_j^ω, i.e. those corresponding to the small-scale features, are not directly observable simply by inverting P, but require the full nonlinear dynamics to be taken into account. Clearly, adopting the wall-based low order modelling approach discussed here completely circumvents the observer design problem, because all the states a_i^τ of the system are directly observable.

5 Conclusions

We have presented a novel methodology for model order reduction of fluid flows that produces low dimensional models that can accurately describe the spatio-temporal evolution of the pressure and shear stress of the surface of a body. In this method, the surface distribution of these two variables is decomposed and represented by a small finite set of wall basis functions, obtained by means of the Proper Orthogonal Decomposition. Subsequently, the methodology reduces to the identification of the coefficients of a dynamical model for the temporal evolution of the amplitudes of the wall shear stress basis functions. The functional form of the dynamical model is a system of ordinary differential equations with quadratic polynomial right-hand-side derived from the vorticity form of the governing equations. In order to produce an accurate estimation of the unsteady forces on the body, the system is complemented with a linear or quadratic data-based model used to estimate the amplitude of the temporal coefficients of the wall pressure basis functions.

In this paper we have applied this methodology to the paradigmatic example modelling the flow past a circular cylinder in the laminar regime. We have shown that a system based on four basis functions for both the shear stress and the pressure is able to accurately describe global features of the flow, such the unsteady forces acting on it, as well as local surface features, like the periodic oscillation of the separation point.

The novelty and fundamental interest with respect to existing methods based on full-field POD Galerkin models can be summarised by the following properties:

- Modelling of complex, three-dimensional unsteady flows might be easier than with standard approaches, because the requirement of detailed full-field measurements can be relaxed to the need of wall measurements only. This is one of the motivations for investigating wall-based models. In addition, this property might simplify the real-time update of the entire model in case where a change of the dynamics occurs as a result of application of flow control or with varying flow conditions.

- All the states of the system constituting the model have a very strong and direct relation with the aerodynamic forces acting on the body. Hence, these wall-based models are well oriented to describe in an accurate manner unsteady loads and fluid structure interactions, especially in the case of fluid induced oscillations, where the body is subject to large displacements. This latter aspect is a current object of research by the authors.

- One further important property of this method is that it circumvents the problem of designing observers to estimate the system states. This is made possible by exploiting the feature that all the states are directly measured, since the wall POD basis functions are obtained as a linear combination of the sensor readings.

Despite these advantages, there remain certain fundamental aspects that are left to future work, that need to be addressed for more complex cases. One major issue, although not observed in the current case, arises from the possible decoupling of the dynamics of coherent structures from their wall signature in more complex flows. In other words, this is because the wall distribution does not, in general, uniquely determines its future evolution, as there might exist more than one flow field with identical wall signature. We argue that the side effect of this phenomenon in our formulation would be a more difficult model identification. A second aspect of major interest will be to include in the model the effects of flow actuation, such that that reduced order controllers that target optimisation of the aerodynamic forces can be designed.

Acknowledgements

Funding from EPSRC under the grants EP/J011126/1, EP/J010537/1, and EP/J010073/1 and support from Airbus Operation Ltd., ETH Zurich (Automatic Control Laboratory), University of Michigan (Department of Mathematics), and University of California, Santa Barbara (Department of Mechanical Engineering) are gratefully acknowledged. The first author is grateful to Prof. Sergei Chernyshenko and Dr. Ati Sharma for fruitful discussions.

References

[1] Bewley TR, Moin P, Temam R. Dns-based predictive control of turbulence: an optimal benchmark for feedback algorithms. *Journal of Fluid Mechanics* 2001; **447**:179–225.

[2] Kim J, Bewley TR. A linear systems approach to flow control. *Annual Review of Fluid Mechanics* 2007; **39**:383–417.

[3] Colburn CH, Cessna JB, Bewley TR. State estimation in wall-bounded flow systems. part 3. the ensemble kalman filter. *Journal of Fluid Mechanics* 2011; **682**:289–303.

[4] Holmes P, Lumley JL, Berkooz G. *Turbulence, coherent structures, dynamical systems and symmetry*. Cambridge university press, 1998.

[5] Cordier L, Noack B, Tissot G, Lehnasch G, Delville J, Balajewicz M, Daviller G, Niven R. Identification strategies for model-based control. *Experiments in Fluids* 2013; **54**(8):1580.

[6] Samimy M, Debiasi M, Caraballo E, Serrani A, Yuan X, Little J, Myatt JH. Feedback control of subsonic cavity flows using reduced-order models. *Journal of Fluid Mechanics* 2007; **579**:315–346.

[7] Berkooz G, Holmes P, Lumley JL. The proper orthogonal decomposition in the analysis of turbulent flows. *Annual Review of Fluid Mechanics* 1993; **25**(1):539–575.

[8] Bergmann M, Cordier L. Optimal control of the cylinder wake in the laminar regime by trust-region methods and pod reduced-order models. *Journal of Computational Physics* 2008; **227**(16):7813 – 7840.

[9] Ravindran S. Reduced-order adaptive controllers for fluid flows using pod. *Journal of Scientific Computing* 2000; **15**(4):457–478.

[10] Bergmann M, Bruneau CH, Iollo A. Enablers for robust pod models. *Journal of Computational Physics* 2009; **228**(2):516 – 538.

[11] Prabhu RD, Collis SS, Chang Y. The influence of control on proper orthogonal decomposition of wall-bounded turbulent flows. *Physics of Fluids (1994-present)* 2001; **13**(2).

[12] Lehmann O, Luchtenburg M, Noack B, King R, Morzynski M, Tadmor G. Wake stabilization using pod galerkin models with interpolated modes. *Decision and Control, 2005 and 2005 European Control Conference. Cdc-Ecc '05*, 2005; 500–505.

[13] Podvin B, Lumley J. Reconstructing the flow in the wall region from wall sensors. *Physics of Fluids (1994-present)* 1998; **10**(5).

[14] Hœpffner J, Chevalier M, Bewley TR, Henningson DS. State estimation in wall-bounded flow systems. part 1. perturbed laminar flows. *Journal of Fluid Mechanics* 2005; **534**:263–294.

[15] Jones BL, Kerrigan EC, Morrison JF, Zaki TA. Flow estimation of boundary layers using dns-based wall shear information. *International Journal of Control* 2011; **84**(8):1310–1325.

[16] Buffoni M, Camarri S, Iollo A, Lombardi E, Salvetti M. A non-linear observer for unsteady three-dimensional flows. *Journal of Computational Physics* 2008; **227**(4):2626 – 2643.

[17] Rowley C, Juttijudata V. Model-based control and estimation of cavity flow oscillations. *Decision and Control, 2005 and 2005 European Control Conference. Cdc-Ecc '05. 44th Ieee Conference on*, 2005; 512–517.

[18] Nagarajan KK, Cordier L, Airiau C, *et al.*. Development and application of a reduced order model for the control of self-sustained instabilities in cavity flows. *Communication in Computational Physics* 2013; **14**.

[19] Kegerise M, Cabell R, III LC. Real-time feedback control of flow-induced cavity tones-part 1: Fixed-gain control. *Journal of Sound and Vibration* 2007; **307**(35):906 – 923.

[20] Hervé A, Sipp D, Schmid PJ, Samuelides M. A physics-based approach to flow control using system identification. *Journal of Fluid Mechanics* 2012; **702**:26–58.

[21] Becker R, King R, Petz R, Nitsche W. Adaptive closed-loop separation control on a high-lift configuration using extremum seeking. *AIAA Journal* 2007; **45**(6):1382–1392.

[22] Gillies E. Low-dimensional control of the circular cylinder wake. *Journal of Fluid Mechanics* 1998; **371**(1):157–178.

[23] Galletti B, Bruneau CH, Zannetti L, Iollo A. Low-order modelling of laminar flow regimes past a confined square cylinder. *Journal of Fluid Mechanics* 2004; **503**:161–170.

[24] Noack BR, Papas P, Monkewitz PA. The need for a pressure-term representation in empirical galerkin models of incompressible shear flows. *Journal of Fluid Mechanics* 2005; **523**:339–365.

[25] Deane AE, Kevrekidis IG, Karniadakis GE, Orszag SA. Low-dimensional models for complex geometry flows: Application to grooved channels and circular cylinders. *Physics of Fluids A: Fluid Dynamics (1989-1993)* 1991; **3**(10):2337–2354.

[26] Noack BR, Afanasiev K, Morzynski M, Tadmor G, Thiele F. A hierarchy of low-dimensional models for the transient and post-transient cylinder wake. *Journal of Fluid Mechanics* 2003; **497**:335–363.

[27] Hay A, Borggaard JT, Pelletier D. Local improvements to reduced-order models using sensitivity analysis of the proper orthogonal decomposition. *Journal of Fluid Mechanics* 2009; **629**:41–72.

[28] Hinze M, Kunisch K. Three control methods for time-dependent fluid flow. *Flow, Turbulence and Combustion* 2000; **65**(3-4):273–298.

[29] Afanasiev K, Hinze M. Adaptive control of a wake flow using proper orthogonal decomposition. *Lecture Notes in Pure and Applied Mathematics* 2001; :317–332.

[30] Bergmann M, Cordier L, Brancher JP. Optimal rotary control of the cylinder wake using proper orthogonal decomposition reduced-order model. *Physics of Fluids (1994-present)* 2005; **17**(9):097101.

[31] Jasak H, Jemcov A, Tukovic Z. Openfoam: A c++ library for complex physics simulations. *International workshop on coupled methods in numerical dynamics*, vol. 1000, 2007; 1–20.

[32] Ferziger JH, Perić M. *Computational methods for fluid dynamics*, vol. 3. Springer Berlin, 2002.

[33] Franke R, Rodi W, Schnung B. Numerical calculation of laminar vortex-shedding flow past cylinders. *Journal of Wind Engineering and Industrial Aerodynamics* 1990; **35**(0):237 – 257.

[34] He JW, Glowinski R, Metcalfe R, Nordlander A, Periaux J. Active control and drag optimization for flow past a circular cylinder: I. oscillatory cylinder rotation. *Journal of Computational Physics* 2000; **163**(1):83 – 117.

[35] Wang Z, Fan J, Cen K. Immersed boundary method for the simulation of 2d viscous flow based on vorticity-velocity formulations. *Journal of Computational Physics* 2009; **228**(5):1504 – 1520.

[36] Lu L, Qin J, Teng B, Li Y. Numerical investigations of lift suppression by feedback rotary oscillation of circular cylinder at low reynolds number. *Physics of Fluids (1994-present)* 2011; **23**(3):033601.

[37] Wu MH, Wen CY, Yen RH, Weng MC, Wang AB. Experimental and numerical study of the separation angle for flow around a circular cylinder at low reynolds number. *Journal of Fluid Mechanics* 2004; **515**:233–260.

[38] Rajani B, Kandasamy A, Majumdar S. Numerical simulation of laminar flow past a circular cylinder. *Applied Mathematical Modelling* 2009; **33**(3):1228 – 1247.

[39] Jordan SK, Fromm JE. Oscillatory drag, lift, and torque on a circular cylinder in a uniform flow. *Physics of Fluids (1958-1988)* 1972; **15**(3):371–376.

[40] Cohen K, Siegel S, McLaughlin T. Sensor placement based on proper orthogonal decomposition modeling of a cylinder wake. *AIAA Paper* 2003; **4259**:2003.

[41] Willcox K. Unsteady flow sensing and estimation via the gappy proper orthogonal decomposition. *Computers & Fluids* 2006; **35**(2):208 – 226.

[42] Rempfer D. On low-dimensional galerkin models for fluid flow. *Theoretical and Computational Fluid Dynamics* 2000; **14**(2):75–88.

[43] Aubry N, Holmes P, Lumley JL, Stone E. The dynamics of coherent structures in the wall region of a turbulent boundary layer. *Journal of Fluid Mechanics* 1988; **192**:115–173.

[44] Rempfer D, Fasel HF. Dynamics of three-dimensional coherent structures in a flat-plate boundary layer. *Journal of Fluid Mechanics* 1994; **275**:257–283.

[45] Sirisup S, Karniadakis GE. A spectral viscosity method for correcting the long-term behavior of pod models. *Journal of Computational Physics* 2004; **194**(1):92–116.

[46] Couplet M, Basdevant C, Sagaut P. Calibrated reduced-order pod-galerkin system for fluid flow modelling. *Journal of Computational Physics* 2005; **207**(1):192 – 220.

[47] Noack BR, Niven RK. Maximum-entropy closure for a galerkin model of an incompressible periodic wake. *Journal of Fluid Mechanics* 2012; **700**:187–213.

[48] Rowley CW. Model reduction for fluids, using balanced proper orthogonal decomposition. *International Journal of Bifurcation and Chaos* 2005; **15**(03):997–1013.

[49] Sirovich L. Turbulence and the dynamics of coherent structures. i-coherent structures. ii-symmetries and transformations. iii-dynamics and scaling. *Quarterly of applied mathematics* 1987; **45**:561–571.

[50] Ma X, Karniadakis GE. A low-dimensional model for simulating three-dimensional cylinder flow. *Journal of Fluid Mechanics* 2002; **458**:181–190.

[51] Perret L, Collin E, Delville J. Polynomial identification of pod based low-order dynamical system. *Journal of Turbulence* 2006; :N17.

[52] Cordier L, Majd E, Abou B, Favier J. Calibration of pod reduced-order models using tikhonov regularization. *International Journal for Numerical Methods in Fluids* 2010; **63**(2):269–296.

[53] Peifer M, Timmer J. Parameter estimation in ordinary differential equations for biochemical processes using the method of multiple shooting. *Systems Biology, IET* 2007; **1**(2):78–88.

[54] Majda AJ, Bertozzi AL. *Vorticity and incompressible flow*, vol. 27. Cambridge University Press, 2002.

[55] Hansen P. Truncated singular value decomposition solutions to discrete ill-posed problems with ill-determined numerical rank. *SIAM Journal on Scientific and Statistical Computing* 1990; **11**(3):503–518.

[56] Graham WR, Peraire J, Tang KY. Optimal control of vortex shedding using low-order models. part ii model-based control. *International Journal for Numerical Methods in Engineering* 1999; **44**(7):973–990.

[57] Bonnet J, Cole D, Delville J, Glauser M, Ukeiley L. Stochastic estimation and proper orthogonal decomposition: Complementary techniques for identifying structure. *Experiments in Fluids* 1994; **17**(5):307–314. URL `10.1007/BF01874409`.

[58] Tinney C, Coiffet F, Delville J, Hall A, Jordan P, Glauser M. On spectral linear stochastic estimation. *Experiments in Fluids* 2006; **41**(5):763–775. URL `10.1007/s00348-006-0199-5`.

[59] Durgesh V, Naughton J. Multi-time-delay lse-pod complementary approach applied to unsteady high-reynolds-number near wake flow. *Experiments in Fluids* 2010; **49**(3):571–583.

[60] Lasagna D, Orazi M, Iuso G. Multi-time delay, multi-point linear stochastic estimation of a cavity shear layer velocity from wall-pressure measurements. *Physics of Fluids (1994-present)* 2013; **25**(1):017101.

[61] Bewley TR, Sharma AS. Efficient grid-based bayesian estimation of nonlinear low-dimensional systems with sparse non-gaussian pdfs. *Automatica* 2012; **48**(7):1286–1290.

[62] Wynn A, Goulart P. Observer design for systems with an energy preserving nonlinearity, with application to fluid flow. *Decision and Control and European Control Conference (Cdc-Ecc), 2011 50th Ieee Conference on*, 2011; 7524–7529.

A Formulation for 3D flows

An ansatz for the three-dimensional velocity vector field is first introduced as

$$\mathbf{u}^N(\mathbf{x},t) = \mathbf{u}_0(\mathbf{x}) + \sum_{i=1}^{N} a_i(t)\mathbf{u}_i(\mathbf{x}), \tag{43}$$

where the vector fields $\mathbf{u}_i(\mathbf{x})$, $i = 1,\ldots,N$, form an orthonormal set of solenoidal basis functions. The transport equation of the vorticity vector $\boldsymbol{\omega} = \nabla \times \mathbf{u}$

$$\frac{\partial \boldsymbol{\omega}}{\partial t} = -(\mathbf{u}\cdot\nabla)\boldsymbol{\omega} + (\boldsymbol{\omega}\cdot\nabla)\mathbf{u} + \frac{1}{Re}\nabla^2\boldsymbol{\omega}, \tag{44}$$

is then projected onto the curl of each of the velocity basis function $\boldsymbol{\omega}_i = \nabla \times \mathbf{u}_i$, $i = 1,\ldots,N$, resulting in a coupled system of N ordinary differential equations

$$\sum_{j=1}^{N} M_{ij}\frac{\mathrm{d}a_j}{\mathrm{d}t} = \sum_{j=0}^{N} L_{ij}a_j + \sum_{j=0}^{N}\sum_{k=0}^{N} N_{ijk}a_j a_k \quad \text{for } i = 1,\ldots,N, \tag{45}$$

where the tensors M_{ij}, L_{ij} are defined as

$$M_{ij} = \int_\Omega \boldsymbol{\omega}_i\cdot\boldsymbol{\omega}_j \mathrm{d}\Omega, \quad L_{ij} = \frac{1}{Re}\int_\Omega \boldsymbol{\omega}_i\cdot\nabla^2\boldsymbol{\omega}_j \mathrm{d}\Omega, \tag{46}$$

and

$$N_{ijk} = -\int_\Omega \boldsymbol{\omega}_i\cdot\Big((\mathbf{u}_j\cdot\nabla)\boldsymbol{\omega}_k - (\boldsymbol{\omega}_k\cdot\nabla)\mathbf{u}_j\Big)\mathrm{d}\Omega. \tag{47}$$

With appropriate initial conditions, equation (45) provides the temporal evolution of the amplitudes $a_i(t)$.

We then introduce a curvilinear local coordinate system (s,l,n) at the wall, with n being the wall normal direction, as in figure 16. The spatio-temporal evolution of the vorticity at the wall is

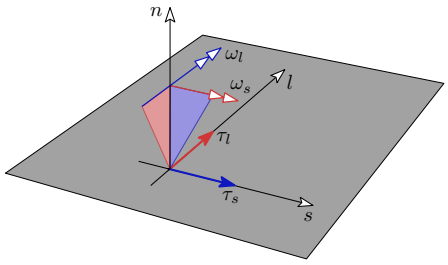

Figure 16: Local coordinate system, vorticity components and viscous shear stresses.

given by

$$\boldsymbol{\omega}^N(s,l,t) = \boldsymbol{\omega}_0(s,l) + \sum_{i=1}^{N} a_i(t)\boldsymbol{\omega}_i(s,l), \tag{48}$$

where the notation $\boldsymbol{\omega}_i(s,l)$ denotes the spatial distribution of the vorticity vector field $\boldsymbol{\omega}_i(\mathbf{x})$ evaluated at the wall. It is easy to show that at the wall the wall-normal component $\omega_i^n(s,l,t)$, where the superscript denotes the component, is identically zero for homogeneous boundary conditions. Hence, for each vorticity basis function as well as for the mean distribution, it holds that

$$\boldsymbol{\omega}_i(s,l) = (\omega_i^s(s,l), \omega_i^l(s,l), 0). \tag{49}$$

According to the reference system in figure 16, the two components of the viscous shear stress at the wall are related to the two components of vorticity as

$$\boldsymbol{\tau}_i(s,l) = \begin{pmatrix} \tau_i^s(s,l) \\ \tau_i^l(s,l) \end{pmatrix} = \frac{1}{Re} \begin{pmatrix} \omega_i^l(s,l) \\ -\omega_i^s(s,l) \end{pmatrix}. \tag{50}$$

It follows that

$$\boldsymbol{\tau}^N(s,l,t) = \boldsymbol{\tau}_0(s,l) + \sum_{i=1}^{N} a_i(t)\boldsymbol{\tau}_i(s,l). \tag{51}$$

Hence, similarly to the 2D case discussed before, the solution of (45) also provides the temporal evolution of the shear stress components at the wall. As a result, the basis functions $\boldsymbol{\tau}_i(s,l)$ can be chosen a priori, and coefficients of a model structure similar to that of equation (45) can be identified from data.